Available online at www.sciencedirect.com
SCIENCE DIRECT
Journal of Solid State Chemistry 179 (2006) 1525–1535
JOURNAL OF SOLID STATE CHEMISTRY
www.elsevier.com/locate/jssc

The intercalation of cetyltrimethylammonium cations into muscovite by a two-step process: II. The intercalation of cetyltrimethylammonium cations into Li-muscovite

Xiaofeng Yu[a], Liyan Zhao[a], Xiuxiang Gao[b], Xiaoping Zhang[c], Nianzu Wu[a,*]

[a]*State Key Laboratory for Structural Chemistry of Unstable and Stable Species, Institute of Physical Chemistry, Peking University, Beijing 100871, China*
[b]*Laboratory Center, Research Institute of Petroleum Exploration and Development, PetroChina, P.O. Box 910, Beijing 100083, China*
[c]*Electron Microscopy Laboratory, Peking University, Beijing 100871, China*

Received 8 December 2005; received in revised form 1 February 2006; accepted 5 February 2006
Available online 10 March 2006

Abstract

The alkylammonium cations were successively intercalated into the interlayer of muscovite. It was achieved by inorganic–organic ion exchange in the hydrothermal reaction of the $LiNO_3$-treated muscovite with cetyltrimethylammonium bromide solution. One-dimensional Patterson plots and electron density calculations show that hydrated Li^+ and CTA^+ cations entered the interlayer of muscovite successively. The CTA^+-intercalated muscovite was characterized by powder X-ray diffraction and elemental analysis, in conjunction with FTIR, nuclear magnetic resonance, X-ray photoelectron spectra, high-resolution transmission electron microscopy, etc. The experiments show that organo-muscovite composite with ordered structure has been obtained. The CTA^+ headgroups are distributed in the interlayer uniformly. However, the arrangement and conformation of CTA^+ chains are strongly dependent upon the reaction temperature. At lower reaction temperature, the chains of CTA^+ ions adopt a little more disordered arrangement and have higher *gauche*/*trans* conformer ratio, resulting in the disturbance to the interlayer symmetry. Whereas at higher reaction temperature, the sample with paraffin-like arrangement of CTA^+ chains could be obtained, in which the methylene chains of CTA^+ adopt a fully stretched, all-*trans* conformation.

Keywords: Layered silicate; Muscovite; Ion exchange; Intercalation; CTAB

1. Introduction

Layered compounds have attracted increased research attention due to their applications in many fields. The intercalation of organic species into the interlayer space of layered silicate has been studied extensively because the resulting intercalates have interesting properties and have many applications in a range of key areas, such as adsorbents for organic pollutants [1], catalysts [2], rheological control agents [3], reinforcement phase in polymer matrices [4], drug carrier in pharmaceutical field [5], photofunctional materials [6], etc.

The ion-exchange intercalation of organic cations into silicate is a result of interplay of several factors: the density of layer charge, the degree of exchange, the length of the alkyl chain, and the host–guest and guest–guest interactions [7,8]. In the 2:1 layered silicate, smectite and vermiculite have been most investigated as host materials in the intercalation because of their swelling behavior and ion-exchange properties [9]. However, another important silicate group, mica (especially muscovite), has attracted much less attention. Muscovite is a clay mineral of special interest because of its well-defined crystal structure, molecularly smooth surface, and outstanding corona resistance [10]. Muscovite belongs to monoclinic structure with the space group ($C2/c$), with the cell parameter $a = 5.18$ Å, $b = 8.99$ Å, $c = 20.07$ Å, and $\beta = 95.75^\circ$ [11].

*Corresponding author. Fax: +86 10 62754943.
E-mail address: wunz@pku.edu.cn (N. Wu).

0022-4596/$ - see front matter © 2006 Elsevier Inc. All rights reserved.
doi:10.1016/j.jssc.2006.02.007

There are two aluminosilicate layers along the [001] direction in one cell unit. Although muscovite belongs to 2:1 phyllosilicate, it has a few distinct differences compared with smectite and vermiculite. First of all, it has very high layer charge density of $2e$ in half unit cell $[O_{20}(OH)_4]$; secondly, it has homogeneous charge distribution; in addition, its layer charge comes from the outside tetrahedral sheet of the aluminosilicate layer and hence produces much strong electrostatic force to hold aluminosilicate layers and the interlayer cations together. Therefore, muscovite does not swell in water; the ion exchange and intercalation, which smectite and vermiculite groups usually have, is not so easy for muscovite. Considering the unique characteristics of muscovite, it will be very interesting if the organic compound intercalation based on muscovite could be obtained.

Unlike smectite and vermiculite, the ion exchange of muscovite was not easily performed. We developed a new method to replace the interlayer cations in muscovite with Li^+ by melting $LiNO_3$ [12]. In the $LiNO_3$ treatments, the spacing of (001) plane $d_{(001)}$ of muscovite was enlarged, providing the possibility for the intercalation of organic cations. In the present paper, alkylammonium intercalation reaction under hydrothermal conditions was put forward. It is well known that alkylammonium cations are easily adsorbed on single-crystal muscovite surface forming stable aggregates of different geometries [13]. It will be interesting to know the condition of alkylammonium intercalated in the interlayer of muscovite. In the present part, we prepared the organo-muscovite composites and aimed to describe microstructural characteristics of alkylammonium-modified muscovite.

2. Experimental

2.1. The $LiNO_3$ treatment of muscovite

The chemical formula of the original muscovite powder ($2M_1$, from Nanling region, China) is $(K_{1.7}Na_{0.3})(Al_{3.54}Fe_{0.26}Mg_{0.20})(Si_{6.20}Al_{1.80})O_{20}(OH)_4$. Muscovite powder (10 g) and $LiNO_3$ powder (170 g) were mechanically mixed. After complete mixing, the mixture was heated in furnace at 300 °C for 12 h. The resulting product was washed with deionized water and filtered, and then dried at 110 °C. The $LiNO_3$ treatment was repeated for seven times. The product is named Li-muscovite.

2.2. The intercalation of Li-muscovite with cetyltrimethylammonium cations

The preparation of surfactant muscovite was undertaken by two methods: one is the hydrothermal reaction method and the other is conventional method. First, 3.0 g cetyltrimethylammonium bromide (CTAB) was dissolved in 50 mL of deionized water, and then 0.5 g of Li-muscovite was mixed with the CTAB solution. To ensure the utmost extent of ion exchange, excessive amount of CTAB has been used. For the hydrothermal reaction, the mixtures were put in a hydrothermal reactor (100 mL) of Teflon-lined stainless-steel autoclave and then heated at different temperatures (80, 120, 150, 180, and 200 °C) for 12 h. For conventional method, the reaction mixture (3.0 g CTAB and 0.5 g Li-muscovite in 100 mL deionized water) was put in a flask under stirring with magnetic stirrer at room temperature (25 °C) under atmosphere for 2 weeks. The mixture was filtered every 2 days and the filtration product was mixed with new CTAB aqueous solution and continues stirring. After the reactions, all the surfactant-muscovite products were filtered and then washed three times with ethanol, dried in a vacuum oven at room temperature. The products were named CTA-M-25, CTA-M-80, CTA-M-120, CTA-M-150, CTA-M-180, and CTA-M-200 separately, according to the different reaction temperatures 25, 80, 120, 150, 180, and 200 °C. Another sample that CTA^+ is adsorbed on single-crystal muscovite surface was prepared. The new cleaved single-crystal muscovite was put in the saturated ethanol solution of CTAB with stirring at room temperature for 12 h, and then took out and washed with ethanol. This sample was named CTA-S.

2.3. Characterization

The powder X-ray diffraction (XRD) patterns were obtained on a Rigaku Rotaflex X-ray powder diffractometer equipped with a graphite-crystal monochromator for Cu$K\alpha$ (Ni filter) radiation. The accelerating voltage was 40 kV and the anode current was 100 mA. The wide-angle diffraction patterns in the 2θ range from 2.5° to 130° were collected with a step size of 0.01° and data acquisition time of 4 s. The small-angle diffraction patterns from 1° to 10° were collected using a step-scanning speed of $0.02^\circ\,s^{-1}$.

Middle-infrared transmission spectra (650–4000 cm^{-1}) were collected using a Nicolet Magna-IR 750 Fourier transform infrared spectrometer equipped with a Nicolet NicPlan IR Microscope operated with a spectral resolution of 4 cm^{-1}.

High-resolution transmission electron microscopy (HRTEM) studies were performed using a Philips Tecnai F30 high-resolution field-emission transmission electron microscope operating at 300 kV, and equipped with energy-dispersive X-ray spectroscopy. TEM samples were prepared by dispersing the powder in alcohol by ultrasonic treatment, dropping onto a porous carbon film supported on a copper grid, and then dried in air.

The elemental analysis of CHN was performed using an Elementar Vario EL instrument. Inductively coupled plasma (ICP) emission spectroscopic data were acquired by ICAP-9000 SP instrument of JARRELL-Ash Company.

^{13}C solid-state nuclear magnetic resonance (NMR) experiments were carried out with a Bruker-AM300 solid-state spectrometer. Samples were loaded into 7 mm zirconia rotors and spun at 4 kHz at room temperature. The ^{13}C CP-MAS spectra were taken at a frequency of

75.47 MHz with the contact time of 1.5 ms and a repetition delay of 3 s. The spectra were externally referenced to hexamethyl-benzene.

X-ray photoelectron spectra (XPS) were acquired with a Kratos Axis Ultra spectrometer operated at 15 kV and 15 mA using an Al$K\alpha$ monochromator. The pressure in the chamber is less than 5.0×10^{-9} Torr. The binding energies were calibrated against the hydrocarbon C1s emission at $E_B = 284.8$ eV.

One-dimensional (1D) Patterson analysis and electron density calculations were carried out based on the powder XRD data. Intensities of $0\,0\,l$ reflections were used for calculations. The 1D Patterson functions were synthesized from $z = -0.2$ to 1.2 in increments of 0.001 for all samples. The structure factors, F, of these reflections were derived from their intensities and corrected for Lorentz-polarization effects according to the following equations:

$$|F(1)| = (I/\mathrm{Lp})^{1/2}, \tag{1}$$

$$\mathrm{Lp} = \frac{1 + \cos^2 2\theta_M \cos^2 2\theta}{2\sin^2\theta \cos\theta(1 + \cos^2 2\theta_M)}, \tag{2}$$

where I is the integrated peak intensity, Lp the Lorentz-polarization factor, and θ_M the diffraction angle of graphite-crystal monochromator. 1D Patterson function values for all samples were calculated as

$$P(z) = 2/c \sum |F(1)|^2 \cos(2\pi lz). \tag{3}$$

Atomic scattering factors for Si, Al, O, K, and Li were determined using

$$f(\theta) = \left[\sum a_i \exp(-b_i \lambda^{-2} \sin^2\theta) + c\right] \exp(-B \sin^2\theta/\lambda^2), \tag{4}$$

where the values a_i, b_i, and c for each element were taken from the literature [14].

The temperature factor B is fixed at 2.0 for all atoms. The structure factors were calculated according to the following equation:

$$F(l) = \sum 2f_i \cos(2\pi l z_j), \tag{5}$$

where f_i is the atomic scattering factor of jth atom, l the Miller indices, and z_j the fractional coordinate on the c-axis.

1D electron density plots were obtained using the following equation:

$$\rho(z) = (1/L)\left[F_0 + 2\sum F_1 \cos(2\pi lz)\right]. \tag{6}$$

3. Results and discussions

3.1. ICP and CHN elemental analysis

After hydrothermal reaction, the chemical composition of the aluminosilicate layer remains the same as original muscovite; however, about 40–50% of the inorganic cations located in the interlayer of Li-muscovite is exchanged by CTA^+ cations, as shown in Table 1. Furthermore, all the three kinds of inorganic cations (K^+, Na^+, and Li^+) take part in the exchange and about half amount of every species are replaced by CTA^+.

3.2. X-ray diffraction

After the hydrothermal reaction of Li-muscovite with CTAB at different temperatures, the diffraction peaks of products moved toward low 2θ region compared with Li-muscovite, as shown in Fig. 1 and Table 2. In all these samples, only the diffraction peaks of sample CTA-M-200 can be easily indexed (Supplemental data Table 2). For sample CTA-M-200, the interlayer spacing calculated from the 2θ angles are $d_{002} \approx 2d_{004} \approx 3d_{006} \approx 4d_{008} \approx 5d_{0010} \approx$ 27.4–27.5 Å, indicating that the spacing of (001) plane $d_{(001)}$ is enlarged from 24.16 to 54.9 Å. For other samples, the first strongest peak is similar to the peak d_{002} of CTA-M-200, but the position moves toward high 2θ angle region with the decrease of reaction temperature. For the second strongest peak (d_{004}), not only it moves toward high 2θ angle region, but also its intensity decreases quickly with the decrease of reaction temperature. So the spacing of (001) plane $d_{(001)}$ decreases and the structure becomes more disordered with the decrease of reaction temperature. It could be noticed that the d_{110} diffraction peaks remain unchanged in all the samples, indicating that the intercalation has no effect on aluminosilicate layer.

Furthermore, in the range of 1–10° (2θ degree), two other new peaks occur and become more and more evident

Table 1
Chemical formula of samples calculated from ICP and CHN elemental analysis

Sample	Formula of CTA-muscovite
Li-muscovite	$(K_{0.40}Na_{0.08}Li_{1.52})(Al_{3.54}Fe_{0.26}Mg_{0.20})(Si_{6.20}Al_{1.80})O_{20}(OH)_4$
CTA-M-25	$(CTA^+_{0.80}K_{0.25}Na_{0.06}Li_{0.89})(Al_{3.54}Fe_{0.26}Mg_{0.20})(Si_{6.20}Al_{1.80})O_{20}(OH)_4$
CTA-M-80	$(CTA^+_{0.94}K_{0.21}Na_{0.04}Li_{0.81})(Al_{3.54}Fe_{0.25}Mg_{0.21})(Si_{6.19}Al_{1.81})O_{20}(OH)_4$
CTA-M-120	$(CTA^+_{0.99}K_{0.20}Na_{0.03}Li_{0.78})(Al_{3.54}Fe_{0.24}Mg_{0.22})(Si_{6.18}Al_{1.82})O_{20}(OH)_4$
CTA-M-150	$(CTA^+_{0.99}K_{0.20}Na_{0.04}Li_{0.77})(Al_{3.54}Fe_{0.25}Mg_{0.21})(Si_{6.19}Al_{1.81})O_{20}(OH)_4$
CTA-M-180	$(CTA^+_{0.97}K_{0.21}Na_{0.03}Li_{0.79})(Al_{3.54}Fe_{0.26}Mg_{0.20})(Si_{6.18}Al_{1.82})O_{20}(OH)_4$
CTA-M-200	$(CTA^+_{0.98}K_{0.20}Na_{0.03}Li_{0.79})(Al_{3.54}Fe_{0.25}Mg_{0.21})(Si_{6.20}Al_{1.80})O_{20}(OH)_4$

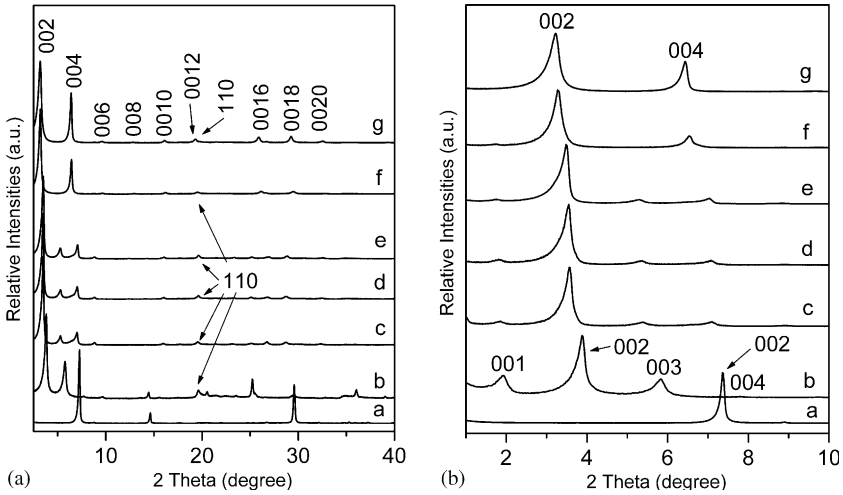

Fig. 1. Powder XRD diffraction patterns of samples: (a) wide-angle diffraction patterns and (b) small-angle diffraction patterns. Letters from a to g represent sample Li-muscovite, CTA-M-25, CTA-M-80, CTA-M-120, CTA-M-150, CTA-M-180, and CTA-M-200, respectively.

Table 2
d-Values of (00*l*) diffraction obtained from small angle XRD patterns

Samples	The *d*-values of (00*l*) diffraction (Å)			
	d_{001}	d_{002}	d_{003}	d_{004}
Li-muscovite		12.1		6.0
CTA-M-25	45.9	22.7	15.2	11.3
CTA-M-80	47.6	24.7	16.3	12.4
CTA-M-120	48.1	24.9	16.5	12.5
CTA-M-150	50.2	25.4	16.7	12.6
CTA-M-180	50.4	26.8		13.4
CTA-M-200		27.4		13.7

with the decrease of reaction temperature, as shown in Fig. 1b. Muscovite belongs to monoclinic crystal system with the space group ($C2/c$) [11]. In this structure, there are two types of symmetry elements related to glide plane: one is *c* glide plane; the other is *n* glide plane. Because of these glide planes, the systematic extinction exists in the (00*l*) diffraction of muscovite, i.e., when the diffraction index *l* is odd, the (00*l*) diffraction intensity is zero. The *c* glide plane and the *n* glide plane are all related to the translation operation along the *c* direction of the unit cell. If any of the symmetry operation is disturbed, the rule of systematic extinction will be invalid and odd (00*l*) diffraction peaks will also appear. Because the inorganic cations in the interlayer are replaced by CTA^+, and the ion exchange has influenced the interlayer spacing dramatically, it is very possible that to some degree the interlayer symmetry along *c* direction is disturbed. So the odd (00*l*) diffraction peaks appear.

3.3. High-resolution transmission electron microscopy

To observe the microstructural change of the products, HRTEM images of ultrathin section were obtained, as shown in Fig. 2. The ultramicrotome section perpendicular to the (001) plane of original muscovite suggests after the hydrothermal reaction the products are still composed of parallel, compact and continuous layers with homogeneous spacing. The HRTEM image of original muscovite shows a spacing of 10 Å, which is in agreement with its d_{002} value. For sample CTA-M-120, the interlayer spacing increased greatly from 10 to 22 Å, which is very near the *d*-value of the strongest diffraction peak (24.9 Å). It could be conjectured that the strongest peak of CTA-M-120 is attributed to the d_{002} diffraction. Fig. 2c shows the image of sample CTA-M-200 with spacing (25 Å), which also can be ascribed to its d_{002} diffraction. However, the interlayer spacings are a little lower than the values obtained from XRD experiment. Such a difference might be due to the sample preparation process for ultrathin section or to the collapse of layers by electron bombardment during HRTEM observations [15]. So HRTEM images clearly show that the interlayer spacing of aluminosilicate layer was enlarged, furthermore, rather ordered layered structure formed after the reaction.

3.4. 1D Patterson analysis and electron density calculations

It seems that the CTA^+ cations could be intercalated in the interlayer of muscovite from XRD and HRTEM results. It is necessary to confirm this by more analysis. We carry out structural analysis of intercalated samples based on the 0 0 *l* reflection via Fourier transform analysis. For this purpose, 1D Patterson function and electron density plots were calculated along the layer stacking direction (*c*-axis) [16].

Fig. 3 shows the 1D Patterson map synthesized from powder XRD data (Supplemental data Tables 1 and 2). Because there are many atoms in one unit cell, some peaks (especially with very wide width) are the overlapping of several vectors. For plot *a*, there are two relative sharp peaks P1 and P2 at $z = 0.19$ and 0.31 (about 4.0 and 6.0 Å),

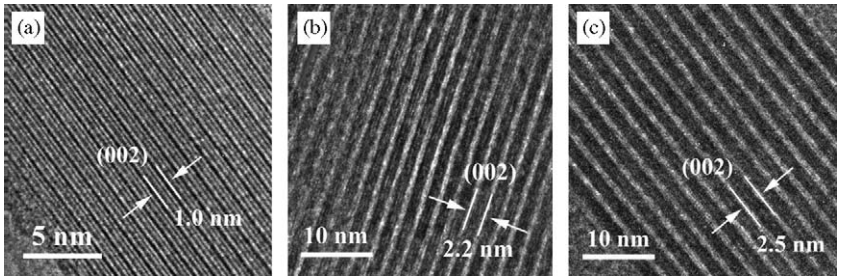

Fig. 2. HRTEM images of samples in ultrathin section of (a) original muscovite, (b) CTA-M-120, and (c) CTA-M-200.

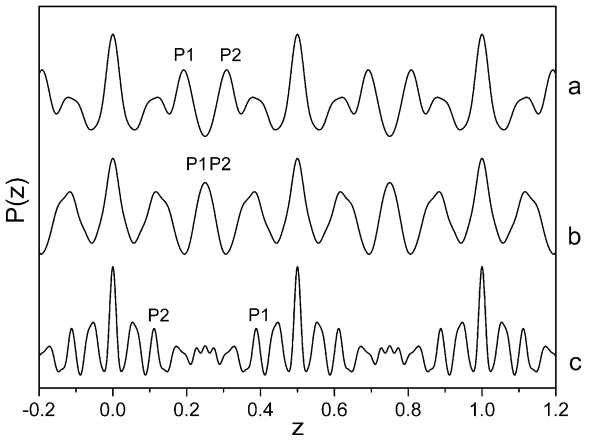

Fig. 3. 1D Patterson function plots along *c*-axis for samples: (a) original muscovite, (b) Li-muscovite, and (c) CTA-M-200.

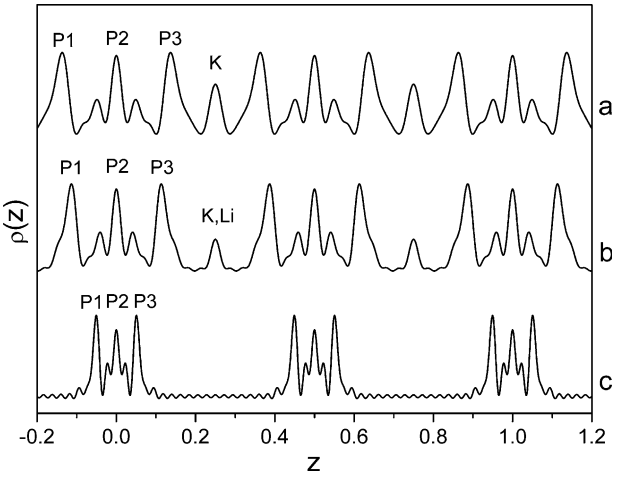

Fig. 4. 1D electron density plots for samples: (a) original muscovite, (b) Li-muscovite, and (c) CTA-M-200.

respectively. According to the structure of muscovite, P1 is attributed to the O–Si vector between surface oxygen and silicon in the neighboring aluminosilicate layer while P2 represents the O–Si vector between surface oxygen and silicon on the other side in the same aluminosilicate layer (Supplemental data Fig. 1). For Li-muscovite, P1 and P2 overlapped at $z = 0.25$ (6.0 Å), indicating the interlayer spacing of muscovite is enlarged about 2.0 Å, which is in agreement with the XRD results; on the other hand, the thickness of aluminosilicate layer remain the same. For plot *c*, the O–Si vector (P2) still remains unchanged at 6.0 Å ($z = 0.11$); while P1 increased to 21.5 Å ($z = 0.39$), indicating that the increment of interlayer spacing is 17.4 Å (also is in agreement with XRD results). Thus, the 1D Patterson function shows that after the $LiNO_3$ treatment, the interlayer spacing was enlarged about 2.0 Å by the hydrated Li^+; after the reaction with CTAB, the interlayer spacing increased dramatically by the intercalation of CTA^+ cations. During the whole process, the aluminosilicate layer did not be affected.

The 1D electron density calculations were carried out, as shown in Fig. 4. For plot *a*, three strong peaks (P1, P2, and P3) centered at $z = -0.137$, 0, and 0.137 (−2.7, 0, and 2.7 Å) represent Si sheet, Al sheet, and Si sheet in aluminosilicate layer. Another peak positioned at $z = 0.25$ indicates K sheet in the interlayer. For Li-muscovite, although the interlayer spacing is enlarged, the three peaks did not change; the intensity of peak at $z = 0.25$ decreased because most of K^+ are replaced by Li^+. For plot *c*, the P1, P2, and P3 still remained at −2.7, 0, and 2.7 Å, respectively, and the interlayer spacing increased greatly, indicating the intercalation of CTA^+ cations. However, the peak at $z = 0.25$ disappeared. Because of the huge interlayer spacing, the rest inorganic cations were probably located near the surface of aluminosilicate layer, the intercalated CTA^+ cations occupied the interlayer space.

From 1D Patterson analysis and 1D electron density calculation, it could be concluded that after the two-step process, most K^+ were replaced by hydrated Li^+ and CTA^+ cations successively, with the aluminosilicate layer remaining unchanged.

3.5. Infrared spectra

Infrared spectroscopy has been deeply related to the studies of structural features, such as chain conformation, chain packing, and even specific conformational sequence. Fig. 5a and Table 3 show the methyl and methylene stretching vibration modes. The bands at around 2918 and 2850 cm^{-1} arise from the CH_2 asymmetric (ν_{as} CH_2) and symmetric (ν_s CH_2) stretching vibration modes of alkyl chain, respectively. The bands around 2946 and 2871 cm^{-1} are due to the asymmetric and symmetric stretching modes of terminal $-CH_3$ group, respectively. It is well known that

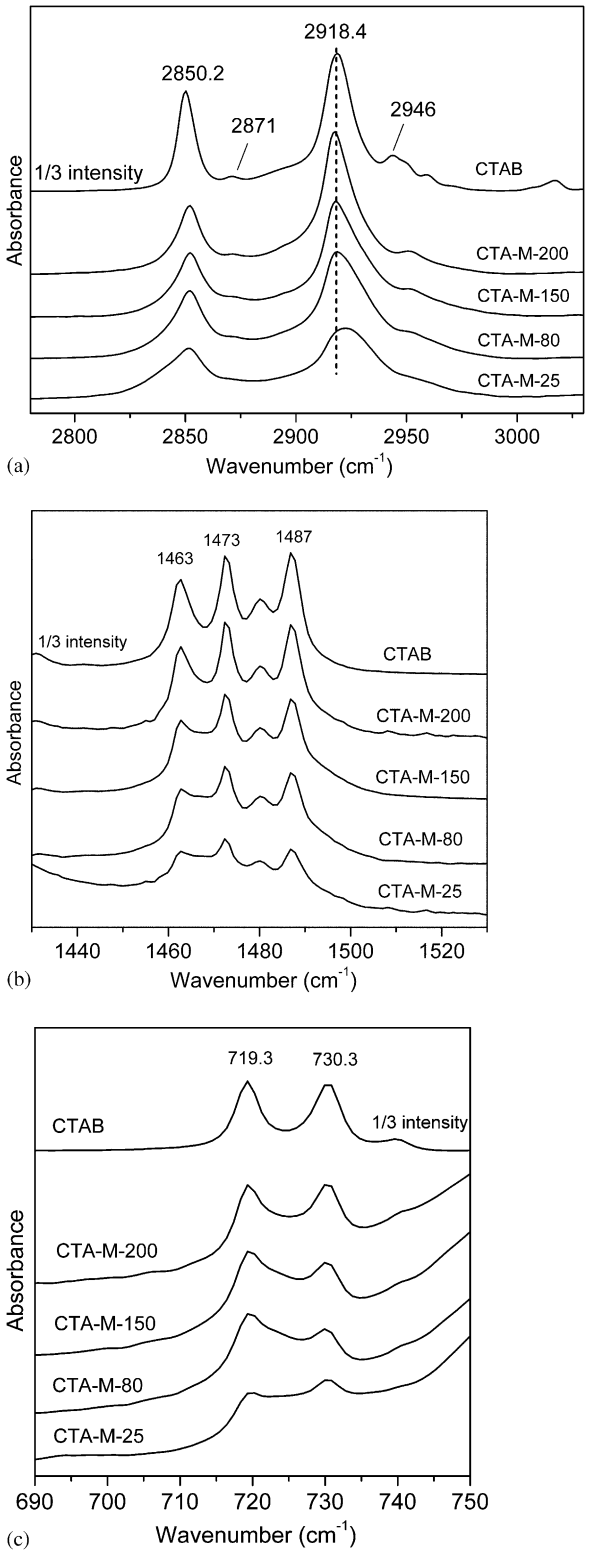

Fig. 5. Selected regions of FTIR absorbance spectra of CTAB and samples: (a) methyl and methylene stretching vibration region, (b) methylene scissoring vibration and asymmetric bending mode of the head $[(CH_3)_3N^+–]$ methyl group, and (c) methylene rocking mode.

the frequency and width of the CH_2 stretching vibration mode are sensitive to the *gauche*/*trans* conformer ratio of methylene chains [8,17–19]. For the all-*trans* alkyl chain,

Table 3
Frequency and FWHM of FTIR methyl and methylene stretching bands for CTAB and CTA-intercalated muscovite

Sample	ν_{as} CH_2 (cm^{-1})		ν_s CH_2 (cm^{-1})	
	Frequency	FWHM	Frequency	FWHM
CTA-M-25	2922.3	27.1	2851.8	20.0
CTA-M-80	2919.2	24.5	2851.8	15.5
CTA-M-150	2918.8	20.0	2851.8	14.2
CTA-M-200	2918.4	16.1	2851.8	11.6
CTAB	2918.4	15.5	2850.2	9.0

ν_{as} CH_2 and ν_s CH_2 represent CH_2 asymmetric stretching vibration and symmetric stretching vibration, respectively. FWHM, full-width at half-maximum.

such as in crystalline CTAB, the positions of CH_2 asymmetric and symmetric stretching mode are at around 2918 and 2850 cm^{-1}, respectively, as shown in Fig. 5a. If conformational disorder is included in the chains, their positions shift to higher wavenumber, depending upon the average content of *gauche* conformers. For example, in the disordered liquid phase of *n*-alkyl chain, the typical positions are in the range of 2856–2858 and 2924–2928 cm^{-1} for the CH_2 symmetric and asymmetric stretching mode [20]. Increased number of *gauche* conformers in the methylene chain is also reflected in an increased line width for these bands. For sample CTA-M-25, many methylene units of CTA^+ chains adopt the *gauche* conformation. With the increase of reaction temperature, the frequency of CH_2 asymmetric stretching mode shifts to lower wavenumber, with its line width becoming smaller. At higher reaction temperature, for sample CTA-M-200, the close proximity of CH_2 asymmetric stretching mode to that of crystalline CTAB indicates that the CTA^+ chains adopt a highly stretched all-*trans* conformation.

Figs. 5b and c show the infrared absorption bands at 1450–1480 and 710–740 cm^{-1}, corresponding to the methylene scissoring mode and methylene rocking mode. The methylene scissoring and rocking modes are sensitive to the interchain interactions and are diagnostic of the packing arrangements in alkyl chain assemblies [21]. For crystalline CTAB, these bands split into two bands, at 1463 and 1473 cm^{-1} for the scissoring mode, and at 719.3 and 730.3 cm^{-1} for the rocking mode. The splitting of the methylene scissoring and rocking band is due to the intermolecular interaction between the two adjacent hydrocarbon chains [21], and further requires an all-*trans* conformation for its detection [22]. For sample CTA-M-25, it has the weaker intensity compared with other samples in both the scissoring and rocking mode, which is consistent with its lowest CTA^+ content. Although the weak intensity for CTA-M-25, the splitting exists and is resolved, indicating the arrangement of CTA^+ chains is not bad. Furthermore, they have the same frequencies as crystalline CTAB in both the scissoring and rocking modes; and the

shape of the bands becomes more and more similar to crystalline CTAB with the increase of reaction temperature. Especially for sample CTA-M-200, it has almost the same absorption bands as crystalline CTAB. These phenomena indicate that the arrangement of CTA^+ chains becomes more and more ordered with the increase of reaction temperature; highly ordered arrangement of CTA^+ chains could be obtained at higher temperature.

The band at $1487\,cm^{-1}$ in Fig. 5b is assigned to the asymmetric bending mode of the head $[(CH_3)_3N^+–]$ methyl group, which is sensitive to the extent of disorder and the packing of the headgroup [18,23,24]. For all the samples, the asymmetric bending modes of CH_3 are almost the same as crystalline CTAB in both wavenumber and line width, indicating that the headgroups of CTA^+ in all the samples are anchored to the aluminosilicate layers with highly ordered distribution. This is consistent with the high charge density and homogeneous charge distribution of muscovite.

From the FTIR analysis, the arrangement of the intercalated CTA^+ in the interlayer of aluminosilicate could be speculated. The headgroups $[(CH_3)_3N^+–]$ of CTA^+ are anchored to the surface of aluminosilicate layers uniformly. For the sample prepared at room temperature, the chains of CTA^+ ions adopt a little more disordered arrangement, with many *gauche* conformers in them. With the increase of reaction temperature, the arrangement of CTA^+ chains becomes more and more ordered, with the ratio of *trans*/*gauche* conformer increasing gradually. For sample CTA-M-200, it is very possible that the chains adopt highly ordered arrangement and are in a fully stretched all-*trans* conformation.

The XRD analysis shows that the systematic extinction becomes invalid for samples prepared at lower reaction temperature. From FTIR analysis, it is very possible that the interlayer symmetry along *c* direction is disturbed by the disordered interlayer structure. With the increase of the reaction temperature, the interlayer structure becomes more and more ordered, while the disturbance to the interlayer symmetry becomes weaker, systematic extinction functions for sample with highly ordered interlayer structure.

3.6. Nuclear magnetic resonance

The ^{13}C resonance for long carbon chain alkylammonium molecules is sensitive to the difference in conformation and packing in addition to the chemical structure. Fig. 6 shows ^{13}C CP-MAS NMR spectra of crystalline CTAB and CTA-intercalated muscovite. The assignment of carbon resonance is shown in Table 4 [25].

For CTA^+-intercalated samples, the position and the intensity of some carbon resonance are changed. For C_1 resonance, not only its position is shifted downfield from 64.2 to 66.0 ppm, but also its intensity is enhanced, and its width is increased greatly. Also the intensity of the C_N resonance is enhanced in the CTA^+-intercalated sample.

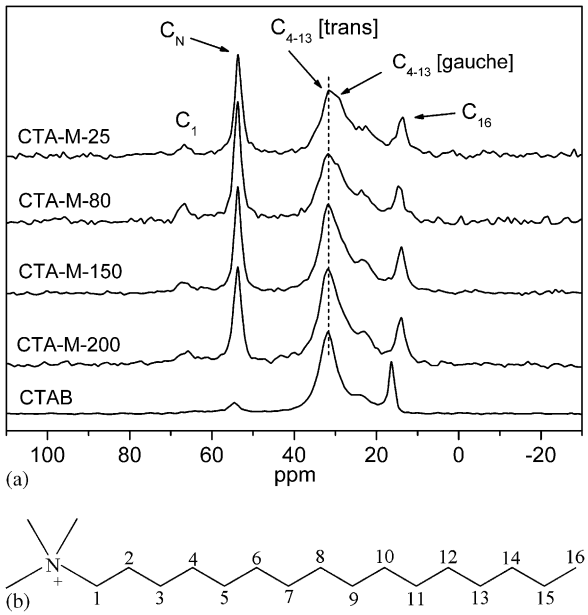

Fig. 6. (a) ^{13}C CP-MAS NMR spectra of crystalline CTAB and samples. (b) All-*trans* molecular structure of CTAB. The carbon atoms are numbered sequentially starting from the methylene carbon attached to the head $[(CH_3)_3N^+–]$ group as shown in the all-*trans* molecule.

Table 4
^{13}C CP-MAS NMR chemical shifts (ppm) of CTAB, CTA-M-200, and CTA-M-25

Carbon atom	CTAB	CTA-M-200	CTA-M-25
C_1	64.2	66.0	65.9
C_N	54.4	53.8	53.9
C_4–C_{13}	32.1	32.1	32.1 (*t*); 29.3 (*g*)
$C_{3,15}$	23.0	23.1	22.8
C_{16}	16.0	14.3	14.5

C_N represents the carbon in the methyl in headgroup $[(CH_3)_3N^+–]$. (*t*) and (*g*) represent *trans* and *gauche*, respectively.

These changes indicate a decreased mobility for the C_1 atom and for the headgroup $[(CH_3)_3N^+–]$ in the intercalated CTA^+ ion [17], showing strong interaction of the CTA^+ headgroup with the aluminosilicate layer. After the intercalation, the CTA^+ is stabilized onto the aluminosilicate surface through cation–anion electrostatic interaction between the headgroup and the oxygen on the aluminosilicate surface, the interaction will be felt more by the C_1 and C_N carbons and then their mobility is considerably declined.

For long alkyl chain surfactants, a ^{13}C NMR signal in the chemical shift range 32–34 ppm indicates the presence of highly ordered all-*trans* domain while a peak in the range 28–30 ppm corresponds to the disordered *gauche* domain in the interior methylene groups of the alkyl group [19,26,27]. For CTA-M-200, the position and width of the C_4–C_{13} remain almost the same as crystalline CTAB, indicating that the methylene carbons of the alkane chains adopt an all-*trans* conformation [17,28,29]. For the others,

a shoulder peak appears at the upfield resonance region (29.3 ppm), and becomes more and more evident with the decrease of the reaction temperature. This indicates a gradual increase in the conformational disorder in the intercalated CTA^+ chains with the decrease of the reaction temperature, which is in agreement with the FTIR results.

For all CTA^+-intercalated samples, the position of C_{16} shifts to upfield from 16.0 to 14.3 ppm, and its peak becomes broader, indicating the decreased mobility at the chain terminal as compared to methyl in crystalline CTAB.

The ^{13}C CP-MAS NMR shows that CTA^+ is anchored to the surface of aluminosilicate through strong cation–anion electrostatic interaction. At the same time, the mobility of the intercalated CTA^+ cation is decreased. For the sample prepared at high temperature, the inner methylenes are in an all-*trans* conformation; with the decrease of reaction temperature, the ratio of *gauche*/*trans* conformer increases.

Because of the disordered conformation of CTA^+ chains, the interlayer symmetry along *c* direction is disturbed to some extent, so the systematic extinction becomes invalid for samples prepared at lower reaction temperature. With the increase of the reaction temperature, the conformational order become better, while the disturbance weakens, systematic extinction functions for the sample with highly ordered interlayer structure.

3.7. X-ray photoelectron spectroscopy

XPS is a well-known technique to probe the chemical composition and structural characteristics of surface species. If an atom layer is covered by an overlayer, the detected photoelectron signal intensity of this atom layer will attenuate during the photoelectron take-off process. The electron inelastic mean free path λ is a criterion to know whether the element under an overlayer could be detected by XPS measurement. The λ is related to the kinetic energy and the kind of overlayer materials. For the CTA^+-intercalated muscovite, the escape depth λ of C1s and N1s core levels is 33.3 and 31.6 Å, respectively [30]. Because the thickness of the muscovite aluminosilicate layer is about 10 Å, the element C and N of intercalated CTA^+, at least in the outmost few layers, could be detected effectively by the XPS measurement.

The C1s and N1s XPS are shown in Figs. 7 and 8. The curve fitting reveals that there are two kind of carbon in pure CTAB. One is the carbon C_2–C_{16} in the alkyl chain [–$(CH_2)_{2-15}CH_3$] according to the assignment shown in NMR plots; the other at higher binding energy is attributed to the carbon around N^+, i.e., [$(CH_3)_3N^+CH_2$–], because nitrogen has higher electronegativity than carbon in the alkyl chain. To compensate for the surface charge effect formed by photoemission, the binding energy was calibrated using hydrocarbon C1s peak at 284.8 eV. Table 5 shows the XPS data of crystalline CTAB, which is in agreement with the data obtained by other authors [31,32]. The atom ratios of C_{2-16}/C_N and C/N calculated from the

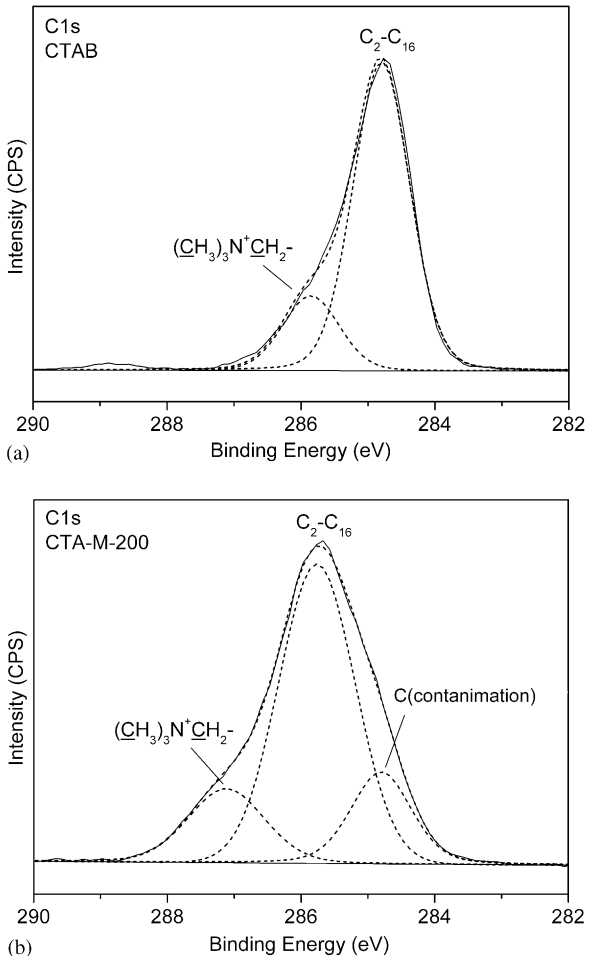

Fig. 7. C1s XP spectra of (a) CTAB and (b) CTA-M-200. The labeled peaks are curve-fitting results for the experimental data.

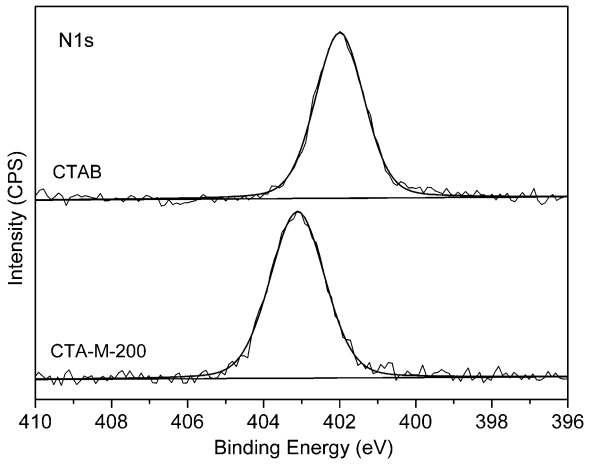

Fig. 8. N1s XP spectra of CTAB and CTA-M-200.

spectra are higher than theoretical number 3.75 and 19, respectively. The reason is that there is usually some contamination hydrocarbon coming from environment, which has the same binding energy as the carbon in the

Table 5
Binding energy and atom ratios of C1s and N1s of crystalline CTAB and CTA-intercalated muscovite

Sample	E_B (C1s) (eV)		E_B (N1s) (eV)	Atom ratio	
	C_2–C_{16}	C_N		C_{2-16}/C_N	C/N
CTAB	284.8	285.8	402.0	4.2*	21.6*
CTA-S	284.8	286.4	402.5	5.4*	21.9*
CTA-M-25	285.7	287.1	403.0	3.8	18.6
CTA-M-80	285.8	287.2	403.1	3.7	18.2
CTA-M-120	285.7	287.0	403.1	3.9	18.9
CTA-M-150	285.8	287.2	403.1	3.7	18.9
CTA-M-180	285.7	287.1	403.0	3.9	18.7
CTA-M-200	285.7	287.1	403.1	3.8	18.2

C_N represents carbon around N^+ in [($\underline{C}H_3)_3N^+\underline{C}H_2$–]. * Presents that the values are higher than theoretical values 3.75 and 19 mentioned in text.

CTA^+ chains, adsorbed onto the sample surface. So the C_{2-16} peak is the overlap of the two kinds of carbon.

After the adsorption of CTA^+ on muscovite surface, the spectra of the C1s and N1s changed greatly (Table 5 and Supplemental data Figs. 2 and 3). For sample CTA-S, the spectrum of N1s moved to higher binding energy, indicating strong interaction between the CTA^+ headgroup and the single-crystal muscovite surface. Because the outmost sheet of the aluminosilicate layer is composed of oxygen anions, the counterion of headgroup is changed from Br^- to oxygen anions. Since oxygen has higher electronegativity than Br^-, the binding energy of N1s increases. Also, the C1s of carbon in [$(CH_3)_3N^+CH_2$–] shifted toward higher binding energy.

However, for intercalated CTA^+, the increase of N1s binding energy is much higher than that of CTA-S, indicating stronger interaction. In the interlayer of muscovite, the chemical environment of the intercalated CTA^+ chains is much different from that on muscovite surface, the CTA^+ cations are placed between aluminosilicate layers, so the binding energy of N1s increased more. For C1s, not only the position of carbon in [$(CH_3)_3N^+CH_2$–], but also in alkyl chain [–$(CH_2)_{2-15}CH_3$] shifted toward higher binding energy. Because about half of the inorganic cations in the interlayer are replaced by CTA^+ cations, the distribution of the CTA^+ is sparse, and the distance between the neighboring CTA^+ chains is very large compared with crystalline CTAB. So the dynamic extra-atomic relaxation energy of discrete molecule following photoemission decreases and the binding energy of carbon of intercalated CTA^+ chains increases dramatically [33]. Because the position of C_{2-16} and C_N all shift to higher binding energy dramatically, the peak of C (contamination hydrocarbon) appears naturally.

XPS measurement shows that after the intercalation a strong interaction happened between the CTA^+ cations and the aluminosilicate layer, through the bonding of [$(CH_3)_3N^+$–] with the oxygen anions. Furthermore, after the measurements for Si2p and Al2p, it has been obtained that there is no substantial difference in both binding energy and shape of peak among original muscovite, Li-muscovite, and CTA^+-intercalated muscovite. This also indicates that not only the $LiNO_3$ treatment, but also the CTA^+ intercalation has no effect on the aluminosilicate layer.

3.8. Discussion

The experiments and 1D Patterson analysis mentioned above show that the CTA^+ could be intercalated into the interlayer of muscovite by a two-step process: inorganic–inorganic and inorganic–organic ion exchange. The structural change originating from the intercalation is of great concern to the interlayer symmetry along *c* direction. For the sample prepared at room temperature, the chains of CTA^+ ions adopt a more disordered arrangement with some *gauche* conformers in them; it is clear that the disorder results in the disturbance to the interlayer symmetry along *c* direction, thus the rule of systematic extinction is invalid and the odd diffraction peaks are prominent. With the increase of reaction temperature, the arrangement of CTA^+ chains becomes more and more ordered, with the ratio of *trans*/*gauche* conformer increasing. For sample CTA-M-200, the chains adopt highly ordered arrangement and are in a fully stretched all-*trans* conformation; the systematic extinction functions and only the even diffraction peaks appear.

The length of the fully stretched CTA^+ is about 23.7 Å, and the cross-sectional diameter of the head of the CTA^+ ion [$(CH_3)_3N^+$–] is about 5 Å. An all-*trans* alkyl chain would occupy a cylindrical volume in space with a cross-sectional diameter of about 2.8 Å. The cell parameters are 5.18 and 9.0 Å, respectively. Because one unit cell is composed of two aluminosilicate layers, so there are two K^+ in one aluminosilicate layer (half unit cell). In the intercalation, about half of the inorganic cations are replaced by CTA^+, so the space in the half unit cell is enough to accommodate it.

According to the analysis of XRD, FTIR, and NMR, the CTA^+ intercalated in sample prepared at low temperature has a higher *gauche*/*trans* ratio. Considering the size of CTA^+ cation, it is impossible for CTA^+ to adopt a lateral monolayer, lateral bilayers arrangements. Because the distribution of the headgroup is uniform and the arrangement of the CTA^+ chains is not so bad, the possible structure of sample obtained at lower temperature is shown in Fig. 9a, which is similar to that proposed by Giannelis and co-workers [8]. The CTA^+ chains adopt a tilted interdigitated array, in which the CTA^+ headgroups are anchored to the opposing aluminosilicate layers and the CTA^+ chains adopt an antiparallel arrangement. Although some *gauche* conformers exist, the chains may adopt a tilted array to some extent. Since the FTIR and NMR analysis show that the ratio of *trans*/*gauche* increases with the increase of reaction temperature, the chain length will slightly increase for the sample prepared at higher

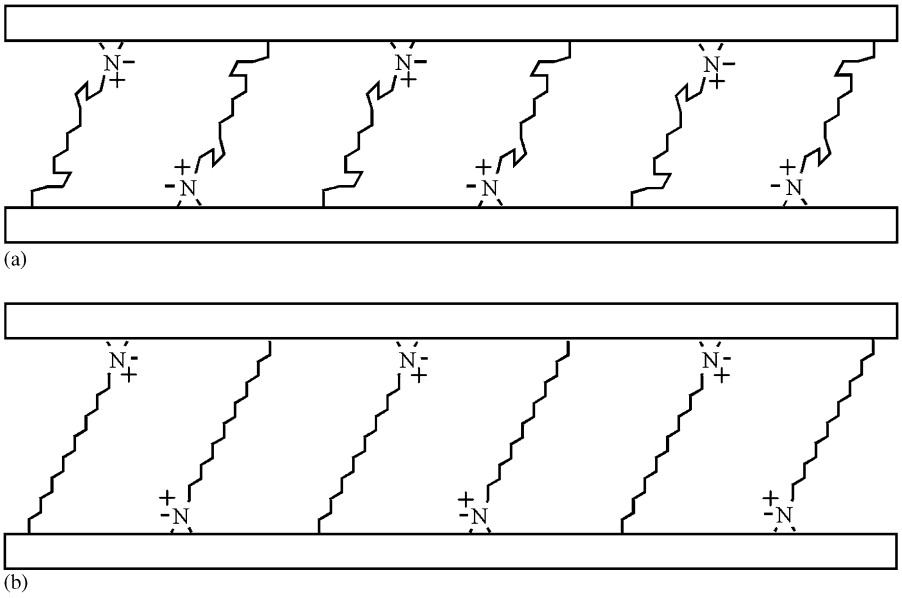

Fig. 9. Possible structure of the intercalated CTA^+ chains in samples: (a) sample prepared at lower temperature and (b) sample CTA-M-200.

temperature, leading to the increase in the interlayer spacing.

For sample CAT-M-200, the *d*-value of its first diffraction peak is 27.4 Å. Because the interlayer spacing (i.e., $d_{002} = d_{(001)}/2$) of original muscovite is 10 Å, after subtracting the diameter of K^+ (3.28 Å), the thickness of aluminosilicate is 6.72 Å. Therefore, the thickness of the CTA^+ molecule layer is 20.68 Å. Fig. 9b shows the structure of sample CAT-M-200, in which the CTA^+ chains adopt a fully extended but tilled position to the surface. Considering the length of CTA^+, the molecular axis of the chains is tilted at an angle of 61° with respect to the aluminosilicate layer. This paraffin-like arrangement is a result of the high charge density, homogeneous charge distribution, layer charge site of muscovite.

Since muscovite is very stable and does not swell like smectite and vermiculite, the first step of inorganic ion exchange is rather important. It provides great possibility for Li-muscovite to be involved in the preparation of various types of new materials. For example, Li-muscovite could be used to prepare polymer-silicate composites, absorbents for toxic organic compounds, intercalated silicate catalysis, drug deliverer [2,4,9], etc. Because of the unique characteristics of aluminosilicate layer in muscovite, the intercalation of muscovite will have prospective applications.

4. Conclusion

The CTA^+-intercalated muscovite composite with ordered structure has been obtained by inorganic–organic ion exchange under hydrothermal condition. The interlayer structure of the CTA^+-intercalated muscovite has been investigated. First, the headgroups of CTA^+ cations were anchored to the surface aluminosilicate layer by strong electrostatic interaction with uniform distribution. Secondly, after the intercalation, the interlayer spacing of aluminosilicate layer was enlarged uniformly. Thirdly, the arrangement and the conformation of CTA^+ chain are strongly related to the reaction temperature. At lower reaction temperature, the arrangement of CTA^+ chain is not very ordered and more *gauche* conformers are present in the CTA^+ chain, leading to the damage of the interlayer symmetry. With the increase of reaction temperature, the arrangement becomes more and more ordered, the ratio of *gauche*/*trans* decreases gradually. For sample prepared at 200 °C, the CTA^+ chains are in a paraffin-like arrangement, and adopt a titled, fully stretched all-*trans* conformation.

Acknowledgments

This project was supported to National Natural Foundation of China (No. 29733080) and the Major State Basic Research Development Program (Grant No. G2000077503).

Appendix A. Supplementary materials

Supplementary data associated with this article can be found in the online version at doi:10.1016/j.jssc.2006.02.007.

References

[1] (a) T. Okada, T. Morita, M. Ogawa, Appl. Clay Sci. 29 (2005) 45–53;
(b) L.P. Meier, R. Nueesch, F.T. Madsen, J. Colloid Interface Sci. 238 (2001) 24–32;
(c) M.R. Stackmeyer, Appl. Clay Sci. 6 (1991) 39–57.
[2] (a) T.J. Pinnavaia, Science 220 (1983) 365–371;
(b) J. Tudor, L. Willington, D. Ohare, B. Royan, Chem. Commun. 17 (1996) 2031–2032;

(c) T. Sivakumar, T. Krithiga, K. Shanthi, T. Mori, J. Kubo, Y. Morikawa, J. Mol. Catal. A. Chem. 223 (2004) 185–194.
[3] E. Manias, G. Hadziioannou, G. Brinke, Langmuir 12 (1996) 4587–4593.
[4] (a) Z. Wang, T.J. Pinnavaia, Chem. Mater. 10 (1998) 3769–3771;
(b) P.C. LeBaron, Z. Wang, T.J. Pinnavaia, Appl. Clay Sci. 15 (1999) 11–29.
[5] (a) T. Tajima, N. Suzuki, Y. Watanabe, Y. Kanzaki, Chem. Pham. Bull. 53 (2005) 1396–1401;
(b) N. Suzuki, Y. Nakamura, Y. Watanabe, Y. Kanzaki, Chem. Pham. Bull. 49 (2001) 964–968;
(c) Y. Kanzaki, Y. Shimoyama, M. Tsukamoto, M. Okano, N. Suzuki, Y. Inoue, T. Tanaka, K. Koizumi, Y. Watanabe, Chem. Pham. Bull. 46 (1998) 1663–1666;
(d) C. Del Hoyo, V. Rives, M.A. Vicents, Clays Clay Miner. 44 (1996) 424–428.
[6] (a) T. Seki, K. Ichimura, Macromolecules 23 (1990) 31–35;
(b) M. Ogawa, K. Kuroda, Chem. Rev. 95 (1995) 399–438.
[7] (a) P. Capkova, H. Schenk, J. Inclusion Phenom. Macrocyclic Chem. 47 (2003) 1–10;
(b) G. Lagaly, A. Weiss, Clays Clay Miner. 20 (1972) 673;
(c) G. Lagaly, Solid State Ionics 22 (1986) 43;
(d) E. Hackett, E. Manias, E.P. Giannelis, J. Chem. Phys. 108 (1998) 7410–7415.
[8] R.A. Vaia, R.K. Teukolsky, E.P. Giannelis, Chem. Mater. 6 (1994) 1017–1022.
[9] (a) M. Ogawa, K. Kuroda, Bull. Chem. Soc. Jpn. 70 (1997) 2593–2618;
(b) S.Y. Lee, W.J. Cho, P.S. Hahn, M. Lee, Y.B. Lee, K.J. Kim, Appl. Clay Sci. 30 (2005) 174–180;
(c) Z. Yermihayu, I. Lapides, S. Yariv, Appl. Clay Sci. 30 (2005) 33–41;
(d) M. Pospisil, A. Kalendova, P. Kapkova, J. Simonik, M. Valaskova, J. Colloid Interface Sci. 277 (2004) 154–161;
(e) A. Perez-Santano, R. Trujillano, C. Belver, A. Gil, M.A. Vicente, J. Colloid Interface Sci. 284 (2005) 239–244;
(f) P. Uthirakumar, C. Kim, K.S. Nahm, Y.B. Hahn, Y.S. Lee, Colloids Surf. A 247 (2004) 69–75.
[10] (a) G.W. Brindly, G. Brown, Crystal Structure of Clay Minerals and their X-ray Identification, Mineralogical Society, Monograph No. 5, London, 1980;
(b) A.C.D. Newman, Chemistry of Clays and Clay Minerals, Mineralogical Society, Monograph No. 6, London, 1987.
[11] J.J. Liang, F.C. Hawthorne, Can. Mineral. 34 (1996) 115–122.
[12] L. Zhao, X. Wang, N. Wu, Y. Xie, Colloid Polym. Sci. 283 (2005) 699–702.
[13] (a) R.E. Lamont, W.A. Ducker, J. Am. Chem. Soc. 120 (1998) 7602–7607;
(b) W.A. Ducker, E.J. Wanless, Langmuir 15 (1999) 160–168;
(c) I.A. Aksay, M. Trau, S. Manne, I. Monma, N. Yao, L. Zhou, P. Fenter, P.M. Eisenberger, S.M. Gruner, Science 273 (1996) 892–898;
(d) S. Manne, H.E. Gaub, Science 270 (1995) 1480–1482.
[14] D.T. Cromer, J.T. Waber, in: J.A. Ibers, W.C. Hamilton (Eds.), International Table for Crystallography, volume IV: Revised and Supplementary Tables, The Kynoch Press, Birmingham, England, 1974.
[15] S.Y. Lee, S.J. Kim, Clays Clay Miner. 50 (2002) 435–445.
[16] (a) S. Sharma, A. Ramanan, M. Jansen, Solid State Ionics 170 (2004) 93–98;
(b) M. Chao, K.D.M. Harris, B.M. Kariuki, C.L. Bauer, B.M. Foxman, J. Phys. Chem. B 106 (2002) 4032–4035.
[17] (a) N.V. Venkataraman, S. Vasudevan, J. Phys. Chem. B 104 (2000) 11179–11185;
(b) N.V. Venkataraman, S. Vasudevan, J. Phys. Chem. B 105 (2001) 1805–1812;
(c) N.V. Venkataraman, S. Vasudevan, J. Phys. Chem. B 105 (2001) 7639–7650;
(d) S. Barman, N.V. Venkataraman, S. Vasudevan, R. Seshadri, J. Phys. Chem. B 107 (2003) 1875–1883.
[18] J.G. Weers, D.R. Scheuing, in: D.R. Scheuing (Ed.), Fourier Transform Infrared Spectroscopy in Colloid and Interface Science, American Chemistry Society, Washington, DC, 1991.
[19] (a) J. Zhu, H. He, L. Zhu, X. Wen, F. Deng, J. Colloid Interface Sci. 286 (2005) 239–244;
(b) Y. Xi, Z. Ding, H. He, R.L. Frost, Spectrochim. Acta A 61 (2005) 515–525.
[20] (a) R.A. MacPhail, H.L. Strauss, R.G. Snyder, C.A. Elliger, J. Phys. Chem. 88 (1984) 334–341;
(b) R.G. Snyder, H.L. Strauss, C.A. Elliger, J. Phys. Chem. 86 (1982) 5145–5150.
[21] (a) R.G. Snyder, J. Chem. Phys. 47 (1967) 1316–1360;
(b) R.G. Snyder, J. Chem. Phys. 71 (1979) 3229–3235;
(c) H.L. Casal, H.H. Mantsch, D.G. Cameron, R.G. Snyder, J. Chem. Phys. 77 (1982) 2825–2830.
[22] C.R. Flach, A. Gericke, R. Mendelsohn, J. Phys. Chem. B 101 (1997) 58–65.
[23] D.R. Scheuing, J.G. Weers, Langmuir 6 (1990) 665–671.
[24] T.C. Wong, N.B. Wong, P.A. Tanner, J. Colloid Interface Sci. 186 (1997) 325–331.
[25] E. Williams, B. Sears, A. Allerhand, E.H. Cordes, J. Am. Chem. Soc. 95 (1973) 4871–4873.
[26] (a) L.Q. Wang, J. Liu, G.J. Exarhos, B.C. Bunker, Langmuir 12 (1996) 2663–2669;
(b) L.Q. Wang, J. Liu, G.J. Exarhos, K.Y. Flanigan, R. Bordia, J. Phys. Chem. B 104 (2000) 2810–2816.
[27] (a) W. Gao, L. Reven, Langmuir 11 (1995) 1860–1863;
(b) A. Badia, W. Gao, S. Singh, L. Demers, L. Cuccia, L. Reven, Langmuir 12 (1996) 1262–1269;
(c) W. Gao, L. Dickinson, C. Grozinger, F.C. Morin, L. Reven, Langmuir 12 (1996) 6429–6435.
[28] D. Kubies, R. Jerome, J. Grandjean, Langmuir 18 (2002) 6159–6163.
[29] H. He, R.L. Frost, F. Deng, J. Zhu, X. Wen, P. Yuan, Clays Clay Miner. 52 (2004) 350–356.
[30] M.P. Seah, W.A. Dench, Surf. Interface Anal. 1 (1979) 2.
[31] G. Beamson, D. Briggs, High Resolution XPS of Organic Polymers: the Scienta ESCA300 Database, 1992.
[32] B.J. Lindberg, J. Hedman, Chem. Scr. 7 (1975) 155–166.
[33] C.D. Wagner, A. Joshi, J. Electron Spectrosc. Relat. Phenom. 47 (1988) 283–313.